MEQNet: Measurement-Efficient Quantum-Inspired Network for Hyperspectral Image Classification

Yuren Chen, Juan Xu*, Sunqi Cai, Mingyuan Pang, Jiawei Xu
Nanjing University of Aeronautics and Astronautics, Nanjing, China
{yurenchen, juanxu, sunqicai, mingyuanpang, xjw1027}@nuaa.edu.cn
*Corresponding author

***Abstract*—Hyperspectral image (HSI) classification leverages the high-dimensional spectral information per pixel to achieve fine-grained identification of objects and land cover. However, its performance is significantly degraded by band redundancy, spectral variability, and class imbalance. Existing deep learning methods often struggle to simultaneously achieve robustness, computational efficiency, and effective suppression of spectral redundancy and variability. Although quantum-inspired learning introduces complex-valued state representations to enhance modeling capacity, it remains sensitive to imbalanced data distributions. To address these challenges, this paper proposes a Measurement-Efficient Quantum-inspired Network, denoted as MEQNet, for robust HSI classification. MEQNet consists of a spectral projection and spatial refinement (SPSR) module and an adaptive complementary measurement (ACM) module to improve numerical stability and reduce computational overhead in quantum-inspired feature fusion. Specifically, SPSR uses a lightweight feature stem to compress the spectral dimension and refine spatial features, reducing spectral redundancy and stabilizing complex-valued state construction. ACM integrates the global low-rank measurement (GLRM) and the local operator measurement (LOM) with a gating-based adaptive selection mechanism, to enhance global representation under class-imbalanced conditions while maintaining lightweight inference under benign scenarios. Experimental results on three HSI datasets demonstrate the superiority of MEQNet over state-of-the-art methods.**

***Index Terms*—Hyperspectral image classification, quantum-inspired learning, complex-valued representation, measurement efficiency.**

I. INTRODUCTION

Hyperspectral images (HSIs) are a class of remote sensing data that capture a continuous and dense spectral signature for each pixel. This distinctive property enables HSI classification to assign land-cover categories by analyzing both spectral and spatial information, facilitating fine-grained object discrimination. HSI classification has been widely adopted in critical applications, including land-cover mapping [1], [2], precision agriculture, environmental monitoring, and urban planning [3]–[5]. With rapid advancements in imaging spectroscopy, modern HSI sensors continue to improve spectral resolution and coverage, providing increasingly rich and accurate information for land-cover classification [6], [7].

However, achieving accurate HSI classification in practical scenarios remains challenging due to several inherent factors: (1) high spectral dimensionality with substantial band redundancy, (2) significant spectral variability caused by illumination changes, atmospheric conditions, and sensor artifacts, and (3) frequent class imbalance in commonly used benchmarks [3], [4]. These factors make spectral–spatial modeling sensitive to noise, prone to biased fitting toward majority classes, and difficult to generalize reliably. For example, on the imbalanced Indian Pines (IP) benchmark, state-of-the-art methods often exhibit a noticeable discrepancy between overall accuracy and class-balanced metrics, as illustrated in Fig. 1. This discrepancy indicates unstable spectral–spatial representations and systematic prediction bias toward majority classes. The inability to reliably capture minority class information exacerbates these challenges, leading to inaccurate predictions, especially under class-imbalanced conditions. Thus, there is a critical need for more robust spectral–spatial fusion mechanisms that can handle these challenges effectively.

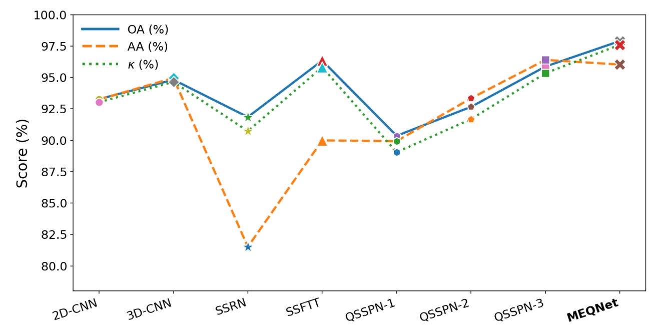

Fig. 1. Performance comparison between the proposed MEQNet framework and existing methods. Classification accuracy metrics on the IP dataset are presented.

Deep learning methods have become the mainstream solution for HSI classification, encompassing various architectures, such as convolutional neural networks (CNNs) with 2D and 3D configurations, and Transformer-based models. 2D CNNs focus mainly on extracting spatial patterns, whereas 3D CNNs jointly model spectral–spatial correlations but often incur higher computational costs and a greater risk of overfitting [8]–[11]. As a result, hybrid 2D–3D CNN architectures are frequently adopted to balance accuracy and efficiency. On the other hand, Transformer-based models capture long-range dependencies through global token interactions [12], [13]. Nevertheless, many existing methods still rely on heavy interaction modules and larger parameter sizes. Under limited-label or imbalanced settings, these approaches can be training-

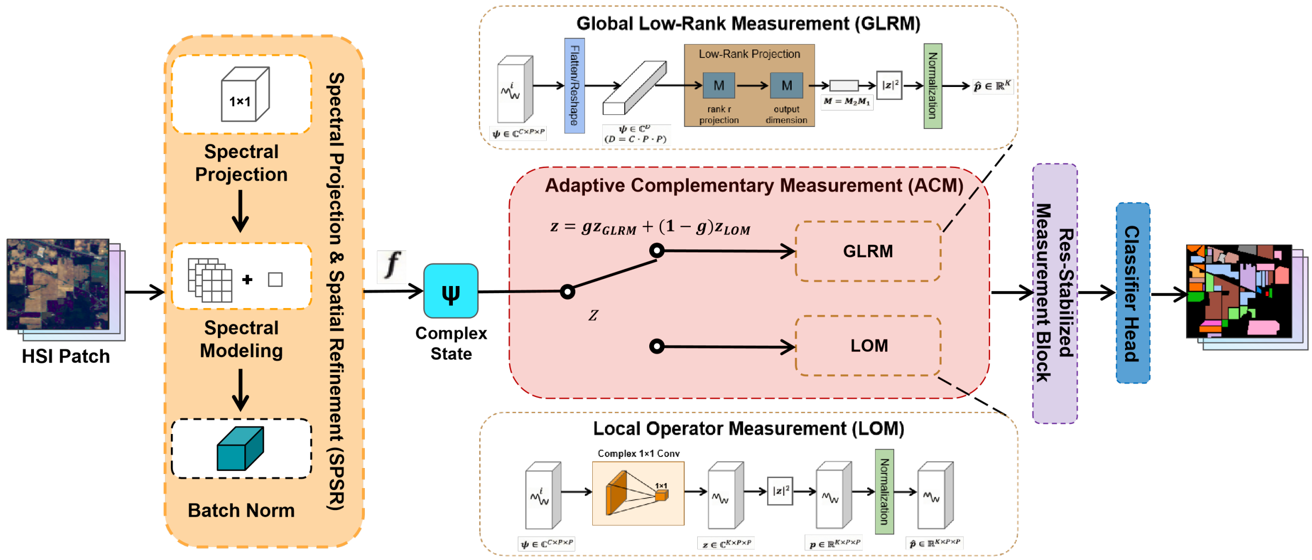

Fig. 2. Illustration of the proposed MEQNet framework. The Spectral Projection and Spatial Refinement (SPSR) is highlighted in the orange box. The middle red box shows the overall Adaptive Complementary Measurement (ACM) module, integrating the upper Global Low-Rank Measurement (GLRM) and Local Operator Measurement (LOM) modules.

sensitive and computationally demanding [14], [15]. In practice, such sensitivity often leads to unstable and class-biased representations, where models overfit majority classes and exhibit significant performance variance across different data splits. This motivates the exploration of more structured and controllable spectral–spatial fusion mechanisms to ensure stable optimization and efficient deployment.

Quantum-inspired learning provides a promising new perspective for HSI classification. The core idea is to map real-valued features into a complex-valued state and then apply a measurement operation to obtain real-valued responses for classification [16], [17]. By introducing amplitude and phase in the complex domain, quantum-inspired learning enables more structured feature interactions. This approach can partially alleviate the negative effects of band redundancy and biased supervision inherent in CNN-based pipelines, thereby mitigating unstable representations and class bias. Quantum-Inspired Spectral-Spatial Pyramid Network (QSSPN) [18] has validated the effectiveness of measurement-driven fusion for HSI classification. However, practical bottlenecks persist in current quantum-inspired approaches. Specifically, modulus-squared readout can lead to training instability under class-imbalanced or small-sample settings. Furthermore, global projection-based measurement often introduces redundant parameters and computational overhead, hindering efficiency and deployability.

To address the aforementioned challenges, we propose the Measurement-Efficient Quantum-inspired Network (MEQNet) to achieve robust HSI classification under imbalanced supervision. Specifically, MEQNet introduces Spectral Projection and Spatial Refinement (SPSR) to compress the spectral dimension and suppress noise via lightweight spatial refinement, producing a more compact and cleaner representation for stable complex-valued state construction. Moreover, MEQNet presents an Adaptive Complementary Measurement (ACM) module to alleviate optimization sensitivity and redundant computation in measurement. ACM contains two complementary branches, namely Global Low-Rank Measurement (GLRM) and Local Operator Measurement (LOM), and employs a gating mechanism to adaptively select between them, enhancing global coupling in imbalanced or challenging settings while maintaining lightweight local inference and reducing redundancy in benign scenarios, achieving a controllable accuracy-efficiency trade-off.

The contributions of this paper are summarized as follows.

- We propose MEQNet, a measurement-efficient quantum-inspired network for HSI classification, which addresses two practical bottlenecks in imbalanced HSI datasets: redundant and noisy feature preparation and optimization instability during the measurement stage.
- MEQNet introduces the SPSR module, which effectively reduces spectral redundancy and noise. This module ensures a compact and stable feature representation, making it well-suited for subsequent quantum-inspired state preparation.
- We present an ACM module that integrates two complementary branches: GLRM and LOM. The gating mechanism allows the network to adaptively select between these two branches, optimizing for global expressiveness in imbalanced settings and computational efficiency in benign scenarios.

II. Method

This section presents the MEQNet framework for HSI classification based on quantum-inspired learning. We first briefly discuss the SPSR module. Then, we describe the proposed ACM module comprising GLRM and LOM branches. At last, we introduce the gating mechanism that adaptively selects and fuses GLRM and LOM pathways based on input HSI feature characteristics for HSI classification. Details of SPSR, ACM, and the gating mechanism are shown in Fig. 2.

A. Spectral Projection and Spatial Refinement (SPSR)

HSI patches are characterized by high spectral dimensionality with strong inter-band redundancy, and the extracted low-level features are often contaminated by local noise. Such redundancy and noise can be amplified in subsequent complex-valued state preparation, making the measurement-driven pipeline more sensitive and harder to optimize. To address these issues, we design a lightweight front-end module, termed SPSR, which performs both spectral compression and spatial refinement to obtain a compact, stable feature representation suitable for quantum-inspired processing.

Given an input HSI patch $\mathbf{x} \in \mathbb{R}^{C \times P \times P}$, SPSR first applies a learnable spectral projection using a 1×1 convolution to reduce the band dimension and aggregate informative spectral responses:

$$\mathbf{x}_s = \sigma(\mathrm{BN}\left(\mathbf{W}_s * \mathbf{x}\right)), \tag{1}$$

where $\mathbf{W}_s$ is the 1×1 convolutional kernel along the spectral dimension, $\mathrm{BN}(\cdot)$ is batch normalization, and $\sigma(\cdot)$ is a nonlinear activation function . This projection reduces redundant spectral components and preserves the discriminative cues, providing a more compact feature representation for the next stage.

Next, SPSR applies a spatial refinement operator to regularize the local neighborhood responses and suppress noise-induced fluctuations:

$$\mathbf{f} = \sigma(\mathrm{BN}\left(\mathbf{W}_{sp} * \mathbf{x}_s\right)), \tag{2}$$

where $\mathbf{W}_{sp}$ is a spatial convolution kernel, and $\mathbf{f} \in \mathbb{R}^{C' \times P \times P}$ is the refined feature map. This spatial refinement mitigates local artifacts and stabilizes feature statistics, which is beneficial for downstream quantum-inspired processing.

After spectral compression and spatial refinement in the SPSR module, the output feature $\mathbf{f}$ is further processed through quantum-inspired state preparation, which encodes the real-valued spectral-spatial features into a complex-valued representation. This complex encoding jointly models the feature *energy* and *relational interactions* via the amplitude-phase mechanism. The amplitude is derived from a normalized energy map, and the phase is predicted through a lightweight module. These amplitude and phase modulations create a structured feature interaction space that supports interference-like coupling, thereby enhancing the measurement-driven feature extraction process. This combination of SPSR and quantum state preparation yields a compact and stable feature map that is well suited for quantum-inspired processing. This design improves downstream classification performance.

Given the output feature $\mathbf{f} \in \mathbb{R}^{C' \times P \times P}$ from SPSR, we prepare the complex state by decoupling $\mathbf{f}$ into a non-negative amplitude map and a bounded phase map:

$$\boldsymbol{\psi} = \mathcal{P}(\mathbf{f}) = \mathbf{A}(\mathbf{f}) \odot e^{i\boldsymbol{\Theta}(\mathbf{f})}, \tag{3}$$

where $\mathbf{A}(\mathbf{f})$ encodes the normalized feature magnitude, and $\boldsymbol{\Theta}(\mathbf{f})$ controls the interaction patterns through phase modulation.

Amplitude preparation. We compute the non-negative energy map via ReLU and normalize it using square-root normalization to obtain the amplitude:

$$\mathbf{A} = \sqrt{\frac{\mathrm{ReLU}(\mathbf{f})}{\sum_{c,u,v} \mathrm{ReLU}(f_{c,u,v}) + \varepsilon}}, \tag{4}$$

where (c, u, v) indexes the channel and spatial positions, and ε is a small constant for numerical stability.

Phase prediction. A lightweight phase-prediction function $\mathcal{G}(\cdot)$ maps $\mathbf{f}$ to a bounded phase:

$$\boldsymbol{\Theta} = \pi \cdot \tanh(\mathcal{G}(\mathbf{f})), \tag{5}$$

ensuring $\boldsymbol{\Theta} \in [-\pi, \pi]$.

Complex state construction. The complex-valued state is then formed as:

$$\boldsymbol{\psi} = \mathbf{A} \odot e^{i\boldsymbol{\Theta}} = \mathbf{A} \odot (\cos\boldsymbol{\Theta} + i \sin\boldsymbol{\Theta}), \tag{6}$$

where $\odot$ denotes the element-wise product. This complex state enables a structured interaction space that facilitates the measurement process in the next stage.

B. Adaptive Complementary Measurement (ACM)

After the quantum-inspired state preparation, MEQNet adopts an ACM module to generate measurement responses that are both expressive and efficient. ACM consists of two complementary branches: GLRM and LOM. GLRM strengthens global spectral–spatial coupling through a low-rank projection, which is particularly beneficial in challenging scenarios where modeling long-range dependencies is important. In contrast, LOM applies lightweight local operators on the complex state to achieve efficient channel-wise mixing, thereby reducing parameters and computation while preserving competitive accuracy in relatively benign cases. By unifying these two complementary branches and allowing their contributions to be adjusted adaptively, ACM provides an effective mechanism to balance representational capacity and inference efficiency within the same measurement pipeline.

1) Gating Mechanism: To adaptively combine GLRM and LOM, ACM introduces a sample-wise gate $\alpha \in [0, 1]$ predicted from the SPSR feature map $\mathbf{f}$. Instead of committing to a single measurement strategy, MEQNet linearly fuses the two branch outputs as

$$\mathbf{z} = \alpha \cdot \mathbf{z}_g + (1 - \alpha) \cdot \mathbf{z}_\ell, \tag{7}$$

where $\mathbf{z}_g$ and $\mathbf{z}_\ell$ denote the measurement responses produced by GLRM and LOM, respectively. Intuitively, a larger α increases the contribution of GLRM to strengthen global dependency modeling for complex inputs, while a smaller α favors the more efficient LOM branch to reduce redundant computation. This gating design enables a controllable accuracy–efficiency trade-off in a simple and effective manner.

TABLE I
CLASSIFICATION RESULTS AND MODEL ANALYSIS OF DIFFERENT METHODS ON HSI DATASETS.

Dataset	Metric	2D-CNN	3D-CNN	SSRN	SSFTT	QSSPN-1	QSSPN-2	QSSPN-3	MEQNet
IP	OA (%)	90.28	92.82	91.85	96.35	90.36	92.66	95.87	**97.90**
	AA (%)	89.25	91.96	81.51	89.99	89.93	93.34	**96.40**	96.03
	κ (%)	89.03	92.65	90.73	95.82	89.05	91.68	95.34	**97.60**
	Params	11.81M	31.74M	735.88K	148.50K	910.50K	1.13M	1.17M	256.38K
	FLOPs	1.80G	182.01G	212.48M	3.66M	34.54M	52.75M	55.59M	40.394M
PU	OA (%)	98.14	98.74	99.63	99.52	99.38	99.44	99.71	**99.88**
	AA (%)	97.12	98.21	99.29	99.20	98.61	98.89	99.43	**99.83**
	κ (%)	97.54	98.65	99.51	99.36	99.17	99.25	99.61	**99.84**
	Params	11.7M	31.4M	396.99K	148.03K	609.16K	666.38K	700.52K	221.38K
	FLOPs	1.80G	182.01G	108.04M	3.66M	10.25M	14.89M	17.66M	37.463M
SA	OA (%)	98.89	98.94	99.31	99.53	99.54	99.63	99.66	**99.89**
	AA (%)	98.89	98.94	99.70	99.72	99.61	99.65	99.81	**99.91**
	κ (%)	98.88	98.94	99.23	99.47	99.49	99.59	99.63	**99.88**
	Params	11.70M	31.4M	750K	148.50K	926.90K	1.16M	1.20M	257.32K
	FLOPs	1.81G	181.79G	216.84M	3.66M	35.87M	54.82M	57.67M	40.545M

2) Global Low-Rank Measurement (GLRM): The GLRM branch captures global spectral–spatial interactions by applying a global low-rank projection to the complex state $\boldsymbol{\psi}$:

$$\mathbf{z}_g = \mathbf{M}\boldsymbol{\psi}_{\text{vec}}, \tag{8}$$

where $\boldsymbol{\psi}_{\text{vec}}$ is the flattened version of the complex state. A low-rank matrix factorization $\mathbf{M}$ is applied to reduce redundancy and preserve global feature correlations, making it suitable for scenarios with complex, imbalanced data. Although it introduces higher computational costs, GLRM enhances global feature representation and is effective when capturing long-range dependencies.

3) Local Operator Measurement (LOM): LOM is designed for computational efficiency, as it avoids global flattening. It applies a local operator directly to the complex state $\boldsymbol{\psi}$:

$$\mathbf{z}_\ell = \mathcal{M}_{\text{loc}}(\boldsymbol{\psi}), \tag{9}$$

where $\mathcal{M}_{\text{loc}}(\cdot)$ represents a lightweight local operation that performs channel-wise mixing at each spatial location. LOM reduces the number of parameters and computational overhead compared to GLRM, making it ideal for lighter and more efficient inference. While it sacrifices some global feature coupling, it maintains efficient performance in less complex scenarios.

GLRM excels in scenarios where capturing global feature dependencies is essential, such as class imbalance or more challenging datasets. On the other hand, LOM is more efficient for scenarios where maintaining lightweight computations is crucial. The adaptive gating mechanism allows MEQNet to select the appropriate measurement strategy based on the data characteristics, achieving a controllable trade-off between accuracy and efficiency.

This adaptive measurement strategy ensures that MEQNet can efficiently handle various HSI classification tasks while providing the necessary flexibility for complex and imbalanced data scenarios.

III. EXPERIMENTAL

A. Experimental Setup and Datasets

Datasets. The proposed method is evaluated on three hyperspectral image datasets, namely IP, Pavia University (PU), and Salinas (SA). Both the IP and SA datasets are acquired by the Airborne Visible/Infrared Imaging Spectrometer (AVIRIS) sensor. Captured over the IP test site in Northwest Indiana, the IP dataset consists of 145×145 pixels and 200 valid spectral bands, with 16 distinct land-cover classes, and suffers from severe class imbalance in its sample distribution. The SA dataset, which covers the SA Valley, contains 512×217 pixels and 204 spectral bands, corresponding to 16 ground-truth categories. Collected by the Reflective Optics System Imaging Spectrometer (ROSIS) sensor over the University of Pavia, the PU dataset comprises 610×340 pixels, 103 spectral bands, and 9 ground-truth classes.

Setup. To evaluate the proposed MEQNet framework, we compare it with several existing methods, including SSFTT [13], 2D-CNN [19], 3D-CNN [20], SSRN [21], and quantum-inspired QSSPN-1, QSSPN-2, and QSSPN-3 [18]. We use the Adam optimizer with a learning rate of 1×10^{-3} and train for 200 epochs with a batch size of 64. The input patch size is $9 \times 9 \times B$, where B denotes the number of spectral bands. We randomly select 10% of the samples for training, 5% for validation, and 85% for testing. Each method is evaluated using overall accuracy (OA), average accuracy (AA), and kappa coefficient (κ), and performance is reported as the average over 10 runs.

B. Classification Results

The experimental results in Table I comprehensively evaluate the classification performance and computational efficiency of eight competing models on three benchmark HSI datasets: IP, PU, and SA. MEQNet achieves the highest OA and κ on all datasets, demonstrating its robustness and superiority in HSI classification. Although the AA is slightly lower on IP

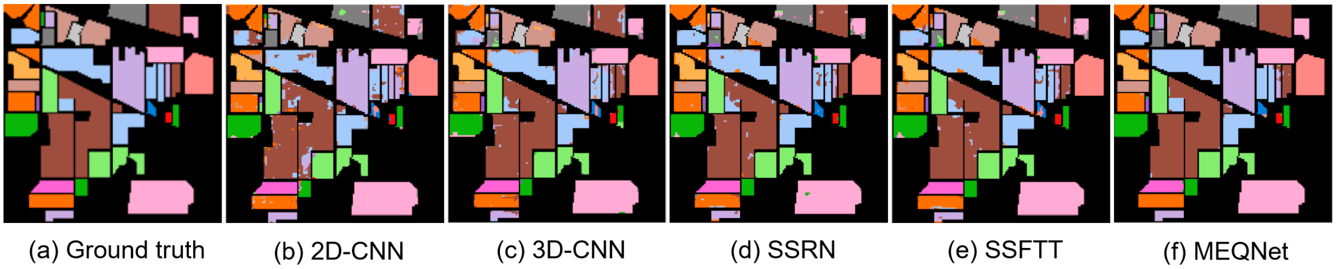

Fig. 3. Classification maps of different methods for the IP dataset.

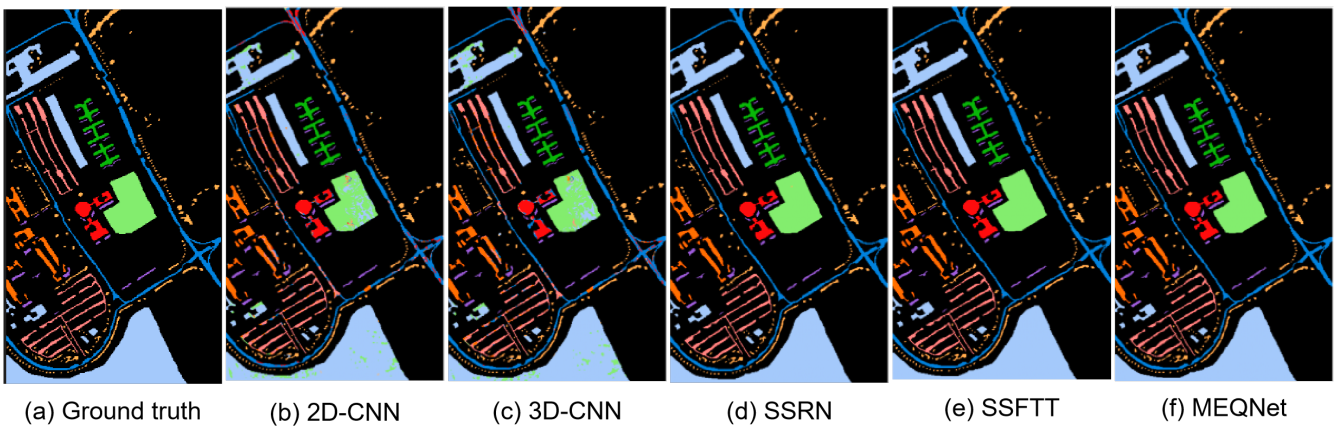

Fig. 4. Classification maps of different methods for the PU dataset.

(96.03%), the overall performance is still superior, particularly given the high class imbalance in this dataset. For the PU and SA datasets, MEQNet outperforms other models with improvements of 0.1% and 0.3% in κ, respectively. These results demonstrate MEQNet's robustness across both imbalanced and balanced datasets.

Regarding computational efficiency, MEQNet maintains a compact model size, with its parameter counts on the three datasets being 1.76M, 3.74M, and 4.05M, respectively, which is significantly lower than that of heavy benchmark models such as 3D-CNN. Its FLOPs are also controlled at a moderate level, effectively balancing precision and computational cost.

As shown in Fig. 3 and Fig. 4, classification maps for the IP and PU datasets are presented, with different methods applied for visualization. These maps highlight the performance of MEQNet in comparison with other methods, showing strong coherence in homogeneous regions and effectively suppressing the noise spots caused by spectral fluctuations in traditional methods. This demonstrates the unique advantage of MEQNet's quantum-inspired interference mechanism in handling complex land-cover boundaries.

Overall, MEQNet demonstrates its effectiveness by maintaining high classification accuracy and computational efficiency, with the ability to handle imbalanced datasets. The combination of high performance and low computational cost makes MEQNet a promising framework for practical hyperspectral image classification.

TABLE II
EFFECTIVENESS OF COMPONENTS ON THE IP DATASET.

Model	Params	FLOPs	OA (%)	κ (%)
MEQNet-Base	22.81M	127.65M	88.92±2.08	89.03±2.21
+SPSR	10.92M	28.84M	97.78±0.24	95.34±0.35
+ACM	0.92M	15.39M	97.81±0.44	97.51±0.50
Full Model	256.38K	40.394M	97.97±0.35	97.69±0.40

C. Ablation Study

Ablation studies are systematically conducted on the IP dataset to empirically validate the efficacy of the proposed SPSR and ACM modules, with quantitative results tabulated in Table II. We denote the baseline setting as MEQNet-Base, which removes all additional components and serves as a reference model for verifying the effectiveness of each component as well as the phase-related design. Upon integrating the SPSR module into the baseline, we observe a substantial improvement in classification performance, with OA increasing significantly, accompanied by a notable reduction in both trainable parameters and FLOPs. Subsequent incorporation of the ACM module further elevates performance, effectively capturing discriminative spatial–spectral correlations. When both modules are combined in the full model, the highest classification accuracy is achieved, with an OA of 97.97% and a Kappa coefficient of 97.69%. Notably, the full model maintains a highly efficient profile, requiring only 256.38K

TABLE III
SENSITIVITY ANALYSIS OF A QUANTUM-INSPIRED BASELINE ON THE IP DATASET.

Model Variant	Phase	Meas. Type	OA (%)
MEQNet-Base	Yes	Complex	88.92
MEQNet-Base w/o Phase	No	Complex	41.92
MEQNet-Base Real-valued	No	Real	39.29

parameters and 40.394M FLOPs. This outcome underscores the synergistic interplay between the SPSR and ACM modules, which not only enhances feature representation but also ensures computational efficiency.

Additionally, the sensitivity analysis of the quantum-inspired engine in Table III provides deeper insights. When the phase information is forcibly removed, resulting in a real-valued network, the model's performance experiences a dramatic drop, with OA plummeting to 41.92%. This phenomenon strongly supports the fact that the phase is not an optional parameter but a core driving force of MEQNet. In high-spectral scenarios with highly overlapping spectral response functions, MEQNet does not rely on increasing network depth to fit the data but instead captures deep, nonlinear physical correlations between materials through phase-encoded interference patterns. This ”phase-driven” feature extraction method causes a severe collapse in the representational space when the core component is removed, further demonstrating the irreplaceability of the proposed quantum-inspired architecture.

IV. CONCLUSION

This paper proposed MEQNet for robust HSI classification, consisting of SPSR and ACM. SPSR employed a lightweight feature stem to compress spectral dimensions and refine spatial features, reducing spectral redundancy and stabilizing complex-valued state construction. ACM integrated GLRM and LOM via a gating-based adaptive selection mechanism to enhance global representation under class-imbalanced conditions while maintaining lightweight local inference in benign scenarios. Extensive experiments on three HSI datasets demonstrated the superiority of MEQNet over state-of-the-art methods in both classification robustness and computational efficiency. In the future, we will investigate more efficient quantum-inspired feature fusion strategies.

ACKNOWLEDGMENT

This work was supported in part by the Quantum Science and Technology-National Science and Technology Major Project (Grant No. 2021ZD0302901), and the National Key Research and Development Program of China (Grant No. 2023YFC3305500).

REFERENCES

[1] Z. Chen, Z. Lu, H. Gao, Y. Zhang, J. Zhao, D. Hong, and B. Zhang, “Global to local: A hierarchical detection algorithm for hyperspectral image target detection,” *IEEE transactions on geoscience and remote sensing*, vol. 60, pp. 1–15, 2022.

[2] J. Yao, D. Hong, C. Li, and J. Chanussot, “Spectralmamba: Efficient mamba for hyperspectral image classification,” *arXiv preprint arXiv:2404.08489*, 2024.

[3] A. Bhargava, A. Sachdeva, K. Sharma, M. H. Alsharif, P. Uthansakul, and M. Uthansakul, “Hyperspectral imaging and its applications: A review,” *Heliyon*, vol. 10, no. 12, 2024.

[4] J. J. Senecal, J. W. Sheppard, and J. A. Shaw, “Efficient convolutional neural networks for multi-spectral image classification,” in *2019 International Joint Conference on Neural Networks (IJCNN)*, 2019, pp. 1–8.

[5] D. Datta, P. K. Mallick, A. K. Bhoi, M. F. Ijaz, J. Shafi, and J. Choi, “Hyperspectral image classification: Potentials, challenges, and future directions,” *Computational intelligence and neuroscience*, vol. 2022, no. 1, p. 3854635, 2022.

[6] A. Bhargava, A. Sachdeva, K. Sharma, M. H. Alsharif, P. Uthansakul, and M. Uthansakul, “Hyperspectral imaging and its applications: A review,” *Heliyon*, vol. 10, no. 12, 2024.

[7] R. Guan, Z. Li, C. Song, G. Yu, X. Li, and R. Feng, “S2rc-gcn: A spatial-spectral reliable contrastive graph convolutional network for complex land cover classification using hyperspectral images,” in *2024 International Joint Conference on Neural Networks (IJCNN)*, 2024, pp. 1–8.

[8] S. Li, W. Song, L. Fang, Y. Chen, P. Ghamisi, and J. A. Benediktsson, “Deep learning for hyperspectral image classification: An overview,” *IEEE transactions on geoscience and remote sensing*, vol. 57, no. 9, pp. 6690–6709, 2019.

[9] X. Yang, Y. Ye, X. Li, R. Y. Lau, X. Zhang, and X. Huang, “Hyperspectral image classification with deep learning models,” *IEEE transactions on geoscience and remote sensing*, vol. 56, no. 9, pp. 5408–5423, 2018.

[10] S. Ghaderizadeh, D. Abbasi-Moghadam, A. Sharifi, N. Zhao, and A. Tariq, “Hyperspectral image classification using a hybrid 3d-2d convolutional neural networks,” *IEEE Journal of Selected Topics in Applied Earth Observations and Remote Sensing*, vol. 14, pp. 7570–7588, 2021.

[11] W. Hu, Y. Huang, L. Wei, F. Zhang, and H. Li, “Deep convolutional neural networks for hyperspectral image classification,” *Journal of Sensors*, vol. 2015, no. 1, p. 258619, 2015.

[12] D. Hong, Z. Han, J. Yao, L. Gao, B. Zhang, A. Plaza, and J. Chanussot, “Spectralformer: Rethinking hyperspectral image classification with transformers,” *IEEE Transactions on Geoscience and Remote Sensing*, vol. 60, pp. 1–15, 2021.

[13] L. Sun, G. Zhao, Y. Zheng, and Z. Wu, “Spectral–spatial feature tokenization transformer for hyperspectral image classification,” *IEEE Transactions on Geoscience and Remote Sensing*, vol. 60, pp. 1–14, 2022.

[14] S. Liu, Q. Shi, and L. Zhang, “Few-shot hyperspectral image classification with unknown classes using multitask deep learning,” *IEEE Transactions on Geoscience and Remote Sensing*, vol. 59, no. 6, pp. 5085–5102, 2020.

[15] A. Afrasiyabi, H. Larochelle, J.-F. Lalonde, and C. Gagné, “Matching feature sets for few-shot image classification,” in *Proceedings of the IEEE/CVF conference on computer vision and pattern recognition*, 2022, pp. 9014–9024.

[16] Y. Li, M. Tian, G. Liu, C. Peng, and L. Jiao, “Quantum optimization and quantum learning: A survey,” *Ieee Access*, vol. 8, pp. 23 568–23 593, 2020.

[17] M. Schuld, I. Sinayskiy, and F. Petruccione, “An introduction to quantum machine learning,” *Contemporary Physics*, vol. 56, no. 2, pp. 172–185, 2015.

[18] J. Zhang, Y. Zhang, and Y. Zhou, “Quantum-inspired spectral-spatial pyramid network for hyperspectral image classification,” in *Proceedings of the IEEE/CVF conference on computer vision and pattern recognition*, 2023, pp. 9925–9934.

[19] S. Yu, S. Jia, and C. Xu, “Convolutional neural networks for hyperspectral image classification,” *Neurocomputing*, vol. 219, pp. 88–98, 2017.

[20] Y. Li, H. Zhang, and Q. Shen, “Spectral–spatial classification of hyperspectral imagery with 3d convolutional neural network,” *Remote Sensing*, vol. 9, no. 1, p. 67, 2017.

[21] Z. Zhong, J. Li, Z. Luo, and M. Chapman, “Spectral–spatial residual network for hyperspectral image classification: A 3-d deep learning framework,” *IEEE transactions on geoscience and remote sensing*, vol. 56, no. 2, pp. 847–858, 2017.